Mechanisms for plasma etching of HfO_2 gate stacks with Si selectivity and photoresist trimming

Juline Shoeb[a)]
Department of Electrical and Computer Engineering, Iowa State University, Ames, Iowa 50011

Mark J. Kushner[b)]
Department of Electrical Engineering and Computer Science, University of Michigan, Ann Arbor, Michigan 48109-2122

(Received 15 June 2009; accepted 24 August 2009; published 21 September 2009)

To minimize leakage currents resulting from the thinning of the insulator in the gate stack of field effect transistors, high-dielectric constant (high-*k*) metal oxides, and HfO_2 in particular, are being implemented as a replacement for SiO_2. To speed the rate of processing, it is desirable to etch the gate stack (e.g., metal gate, antireflection layers, and dielectric) in a single process while having selectivity to the underlying Si. Plasma etching using $Ar/BCl_3/Cl_2$ mixtures effectively etches HfO_2 while having good selectivity to Si. In this article, results from integrated reactor and feature scale modeling of gate-stack etching in $Ar/BCl_3/Cl_2$ plasmas, preceded by photoresist trimming in Ar/O_2 plasmas, are discussed. It was found that BCl_n species react with HfO_2, which under ion impact, form volatile etch products such as B_mOCl_n and $HfCl_n$. Selectivity to Si is achieved by creating Si–B bonding as a precursor to the deposition of a BCl_n polymer which slows the etch rate relative to HfO_2. The low ion energies required to achieve this selectivity then challenge one to obtain highly anisotropic profiles in the metal gate portion of the stack. Validation was performed with data from literature. The effect of bias voltage and key reactant probabilities on etch rate, selectivity, and profile are discussed. © *2009 American Vacuum Society.* [DOI: 10.1116/1.3231480]

I. INTRODUCTION

SiO_2 has long served as the gate insulator for field effect transistors in very-large-scale integrated circuits.[1] As feature sizes decrease, the gate-silicon dioxide equivalent thickness required for the insulator also decreases.[2] A larger oxide capacitance (thinner oxide layer) is necessary to invert the surface to a sufficient sheet charge density to obtain the desired transistor current for a given supply voltage. Continuing to reduce the insulator thickness using SiO_2 is problematic as leakage currents due to tunneling increase as the thickness approaches a monolayer.[1] Consequently, high-dielectric constant (high-*k*) metal oxides and HfO_2, in particular, are being implemented as replacements for SiO_2 in gate stacks to minimize leakage current resulting from thinning of the insulator. The larger dielectric constant allows the oxide to be thicker for a given capacitance, thereby decreasing electric fields and leakage currents.

A high-*k* dielectric and a poly-Si gate are typically not suitable for high performance logic as the combination has a higher threshold voltage and lower channel mobility, and so a poor drive current.[1] Metal gates, having a higher free carrier density, maintain a high mobility at junctions with high-*k* dielectrics and so many advanced designs incorporate metal gates.[1] TiN is one such metal being considered for the gate.[3] Given other technology requirements, such as back-antireflection coatings (BARC) to maintain critical dimensions (CDs) during lithography, the gate stack prior to etching can contain many layers and materials, as schematically shown in Fig. 1.

To speed the plasma processing of gate stacks, it is desirable to etch the entire stack using a single process. This requires a high selectivity for the oxide, in this case HfO_2, with respect to the underlying Si layer. (That is, the HfO_2 will be etched but the underlying Si will not be etched.) It has been found that similar gate stacks can be etched using BCl_3/Cl_2 plasmas while having a good selectivity to underlying Si by forming a BCl_n polymer on the Si which slows its etching.[4]

In this article, the plasma etching of HfO_2 gate stacks is computationally investigated with an emphasis on the selectivity between HfO_2 and Si. The model gate stack consists of photoresist (PR), BARC, TiN, HfO_2, SiO_2, and the underlying Si (see Fig. 1.) This gate stack is based on industrial test structures. Reaction mechanisms for etching of TiN and HfO_2 were developed for plasmas sustained in $Ar/BCl_3/Cl_2$ mixtures. Trimming of the PR to achieve narrower linewidths was also addressed. The Hybrid Plasma Equipment Model (HPEM) was employed to simulate the reactor scale and surface kinetics for inductively and capacitively coupled plasma tools. The model reactor is an inductively coupled plasma (ICP) having a radio frequency (rf) bias on the substrate. The mechanisms were then implemented in the Monte Carlo Feature Profile Model (MCFPM) with which etch profiles are predicted. Validation was performed with data from literature.

We found that BCl_n species produced by electron impact in the plasma react with HfO_2, which under ion impact form

---

[a)] Electronic mail: jshoeb@iastate.edu
[b)] Author to whom correspondence should be addressed; electronic mail: mjkush@umich.edu

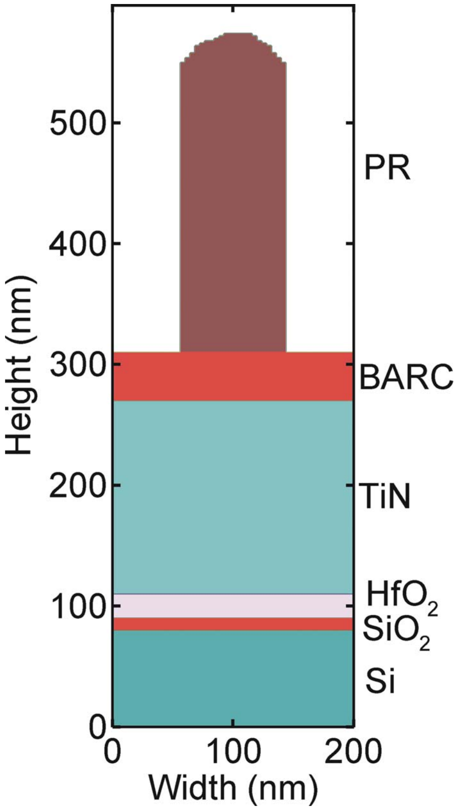

FIG. 1. (Color online) Initial gate stack. The PR width is 58 nm and height is 290 nm. The thicknesses of the layers are BARC 40 nm, TiN 160 nm, HfO_2 20 nm, and SiO_2 10 nm.

volatile etch products such as B_mOCl_n and $HfCl_n$. Selectivity to Si is achieved by creating Si–B bonding as a precursor to the deposition of a BCl_n polymer, which slows the etch rate relative to HfO_2. The low ion energies required to achieve this selectivity then challenge one to obtain highly anisotropic profiles in the metal gate portion of the stack.

The models used in this investigation are briefly described in Sec. II followed by a discussion of the reaction mechanisms in Sec. III. Photoresist trimming and BARC etching are discussed in Sec. IV. Plasma properties and HfO_2 etch characteristics are discussed in Sec. V followed by our concluding remarks in Sec. VI.

II. DESCRIPTION OF THE MODELS

The HPEM was used to predict the reactor scale plasma characteristics and reactant fluxes to surfaces in the ICP reactor. The HPEM has been previously described and so is only briefly summarized here.[5] The HPEM is a two-dimensional (2D), modular model which addresses gas phase and surface kinetics. Electromagnetic fields are derived by solving the frequency domain wave equation based on coil currents adjusted to deliver a specified power deposition. The spatially dependent power deposition is used as a source term in obtaining the electron temperature, T_e, from an electron energy conservation equation. Transport and rate coefficients as function of average electron energy are obtained from a solution of Boltzmann's equation, and a Monte Carlo simulation is used to follow the trajectories of sheath accelerated secondary electrons. The transport coefficients and source functions are used by the fluid kinetics module (FKM) to solve separate continuity, momentum, and energy equations for each ion and neutral species, while semi-implicitly solving Poisson's equation for the time varying electrostatic potential. The densities and electrostatic fields from the FKM are then transferred to the other modules. This process is iterated until a converged quasisteady state solution is obtained.

Reaction probabilities for gas phase species with surfaces are provided by the surface chemistry module (SCM) which computes the composition of surface resident species using a multilayer surface-site-balance model. The reaction mechanism is unique for each surface in contact with the plasma. The plasma chemistry Monte Carlo module (PCMCM) produces the energy and angular distributions for neutrals and ions striking surfaces in contact with the plasma. The PCMCM launches pseudoparticles representing ions and neutrals based on the electron impact source functions. Using time dependent electric fields from the FKM, their trajectories are integrated while accounting for gas phase collisions. The energy and angular distributions (EADs) of ion (IEADs) and neutral pseudoparticles are recorded as they strike surfaces.

The SCM and MCFPM incorporate energy dependent reaction probabilities based on the EADs obtained from the PCMCM. The probabilities for surface reactions involving energetic species (either ions or hot neutrals) are given by[6]

$$p(E) = p_0 \frac{E^m - E_t^m}{E_r^m - E_t^m}, \tag{1}$$

where $p(E)$ is the reaction probability for a particle with energy E, E_t is the threshold energy of the process, E_r is a reference energy, and p_o is the reaction probability at the reference energy. We used $m=0.5$ for sputtering or ion activated etching.

The 2D MCFPM has been previously described and so is briefly summarized here.[7] The MCFPM predicts the evolution of surface morphology and profiles based on the fluxes and EADs from the HPEM. The MCFPM resolves surface materials using a 2D rectilinear mesh where each cell in the mesh is assigned a material identity. Gas phase species are represented by pseudoparticles and surface species are represented by computational mesh cells. Pseudoparticles are launched toward the surface from random locations above the wafer with energies and angles sampled from the EADs. The trajectories of the pseudoparticles are tracked until they hit a surface, where a generalized surface reaction mechanism controls the interaction. The identity of the material mesh cell is changed (representing a surface chemical reaction), removed (etching), or a cell is added (deposition) as dictated by the reaction mechanism. Gas phase pseudoparticles are reflected or emitted from the surface consistent with the mechanism.

The ICP reactor used in this study is schematically shown in Fig. 2(a). The cylindrical chamber is 13 cm in radius and

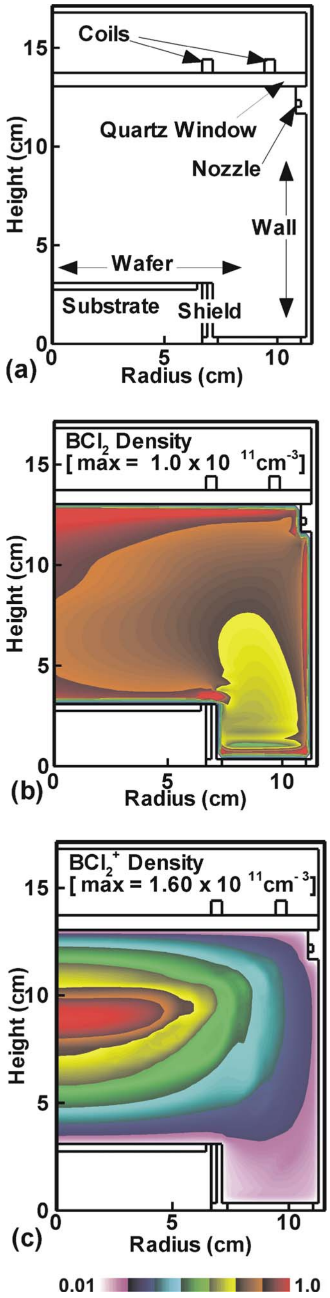

FIG. 2. (Color online) ICP reactor and typical plasma properties for $Ar/BCl_3/Cl_2=5/40/55$, 300 W ICP, 5 mTorr, and 100 SCCM. (a) Schematic of the reactor. (b) BCl_2 density and (c) BCl_2^+ density.

TABLE I. $Ar/BCl_3/Cl_2$ gas phase reaction mechanism (species: Ar, Ar^*, Ar^+, e, Cl_2, Cl_2^+, Cl, Cl^*, Cl^+, Cl^-, BCl_3, BlC_2, BCl_3^+, and BlC_2^+).

Reaction	Rate coefficient	Reference
$e+\mathrm{Ar}\rightarrow\mathrm{Ar}+e$	$f(\varepsilon)$ [a]	14
$e+\mathrm{Ar}\rightarrow\mathrm{Ar}^*+e$	$f(\varepsilon)$ [a]	15
$e+\mathrm{Ar}\rightarrow\mathrm{Ar}^++e+e$	$f(\varepsilon)$ [a]	16
$e+\mathrm{Ar}^*\rightarrow\mathrm{Ar}^++e+e$	$f(\varepsilon)$ [a]	17
$e+\mathrm{Ar}^*\rightarrow\mathrm{Ar}+e$	$f(\varepsilon)$ [a]	18
$e+\mathrm{Cl}_2\rightarrow\mathrm{Cl}_2+e$	$f(\varepsilon)$ [a]	19
$e+\mathrm{Cl}_2\rightarrow\mathrm{Cl}_2(v)+e$	$f(\varepsilon)$ [a]	19,[b]
$e+\mathrm{Cl}_2\rightarrow\mathrm{Cl}+\mathrm{Cl}-$	$f(\varepsilon)$ [a]	19
$e+\mathrm{Cl}_2\rightarrow\mathrm{Cl}+\mathrm{Cl}+e$	$f(\varepsilon)$ [a]	19
$e+\mathrm{Cl}_2\rightarrow\mathrm{Cl}_2^++e+e$	$f(\varepsilon)$ [a]	19
$e+\mathrm{Cl}\rightarrow\mathrm{Cl}+e$	$f(\varepsilon)$ [a]	19
$e+\mathrm{Cl}\rightarrow\mathrm{Cl}^*+e$	$f(\varepsilon)$ [a]	19
$e+\mathrm{Cl}\rightarrow\mathrm{Cl}^++e+e$	$f(\varepsilon)$ [a]	19
$e+\mathrm{Cl}^*\rightarrow\mathrm{Cl}^*+e$	$f(\varepsilon)$ [a]	19
$e+\mathrm{Cl}^*\rightarrow\mathrm{Cl}+e$	$f(\varepsilon)$ [a]	19
$e+\mathrm{Cl}^*\rightarrow\mathrm{Cl}^++e+e$	$f(\varepsilon)$ [a]	19
$e+\mathrm{Cl}-\rightarrow\mathrm{Cl}+e+e$	$f(\varepsilon)$ [a]	19
$e+\mathrm{Cl}_2^+\rightarrow\mathrm{Cl}+\mathrm{Cl}$	$1\times10^{-7}/T_e^{0.5}$	[c]
$e+\mathrm{BCl}_3\rightarrow\mathrm{BCl}_3+e$	$f(\varepsilon)$ [a]	[c]
$e+\mathrm{BCl}_3\rightarrow\mathrm{BCl}_3(v)+e$	$f(\varepsilon)$ [a]	20
$e+\mathrm{BCl}_3\rightarrow\mathrm{BCl}_2+\mathrm{Cl}-$	$f(\varepsilon)$ [a]	20
$e+\mathrm{BCl}_3\rightarrow\mathrm{BCl}_2+\mathrm{Cl}+e$	$f(\varepsilon)$ [a]	21
$e+\mathrm{BCl}_3\rightarrow\mathrm{BCl}_3^++e+e$	$f(\varepsilon)$ [a]	21
$e+\mathrm{BCl}_3\rightarrow\mathrm{BCl}_2^++\mathrm{Cl}+e+e$	$f(\varepsilon)$ [a]	21
$e+\mathrm{BCl}_3^+\rightarrow\mathrm{BCl}_2+\mathrm{Cl}$	$1\times10^{-7}/T_e^{0.5}$	22, [c]
$e+\mathrm{BCl}_2\rightarrow\mathrm{BCl}_2+e$	$f(\varepsilon)$ [a]	[d]
$e+\mathrm{BCl}_2\rightarrow\mathrm{BCl}_2(v)+e$	$f(\varepsilon)$ [a]	[b,d]
$e+\mathrm{BCl}_2\rightarrow\mathrm{BCl}_2^++e+e$	$f(\varepsilon)$ [a]	23
$e+\mathrm{BCl}_2^+\rightarrow\mathrm{BCl}_2$	$1\times10^{-7}/T_e^{0.5}$	22
$\mathrm{Cl}^*\rightarrow\mathrm{Cl}$	1×10^{5}	[c]
$\mathrm{Cl}^-+\mathrm{Cl}^+\rightarrow\mathrm{Cl}+\mathrm{Cl}$	1×10^{-7}	[c]
$\mathrm{Cl}^-+\mathrm{Cl}_2^+\rightarrow\mathrm{Cl}_2+\mathrm{Cl}$	1×10^{-7}	[c]
$\mathrm{Cl}^-+\mathrm{Ar}^+\rightarrow\mathrm{Cl}+\mathrm{Ar}$	1×10^{-7}	[c]
$\mathrm{Cl}^-+\mathrm{BCl}_2^+\rightarrow\mathrm{BCl}_2+\mathrm{Cl}$	1×10^{-7}	[c]
$\mathrm{Cl}^-+\mathrm{BCl}_3^+\rightarrow\mathrm{BCl}_3+\mathrm{Cl}$	1×10^{-7}	[c]
$\mathrm{Ar}^*+\mathrm{Ar}^*\rightarrow\mathrm{Ar}^++e+\mathrm{Ar}$	5×10^{-10}	[c]
$\mathrm{Ar}^*+\mathrm{Cl}_2\rightarrow\mathrm{Cl}_2^++\mathrm{Ar}+e$	7.1×10^{-10}	[c]
$\mathrm{Ar}^*+\mathrm{Cl}\rightarrow\mathrm{Cl}^*+\mathrm{Ar}$	0.7×10^{-11}	[c]
$\mathrm{Ar}^*+\mathrm{BCl}_3\rightarrow\mathrm{BCl}_2+\mathrm{Cl}+\mathrm{Ar}$	1×10^{-11}	[c]
$\mathrm{Ar}^*+\mathrm{BCl}_2\rightarrow\mathrm{BCl}_2^++\mathrm{Ar}+e$	1×10^{-11}	[c]
$\mathrm{Ar}^++\mathrm{Cl}_2\rightarrow\mathrm{Cl}_2^++\mathrm{Ar}$	0.84×10^{-10}	24
$\mathrm{Ar}^++\mathrm{Cl}_2\rightarrow\mathrm{Cl}^++\mathrm{Cl}+\mathrm{Ar}$	0.64×10^{-10}	24
$\mathrm{Ar}^++\mathrm{Cl}\rightarrow\mathrm{Cl}^++\mathrm{Ar}$	2×10^{-10}	24
$\mathrm{Ar}^++\mathrm{BCl}_3\rightarrow\mathrm{BCl}_2^++\mathrm{Cl}+\mathrm{Ar}$	5×10^{-10}	[c]
$\mathrm{Ar}^++\mathrm{BCl}_2\rightarrow\mathrm{BCl}_2^++\mathrm{Ar}$	1×10^{-10}	[c]
$\mathrm{Cl}^++\mathrm{Cl}_2\rightarrow\mathrm{Cl}_2^++\mathrm{Cl}$	5.4×10^{-10}	[c]
$\mathrm{Cl}^++\mathrm{BCl}_3\rightarrow\mathrm{BCl}_2^++\mathrm{Cl}_2$	6.2×10^{-10}	[c]
$\mathrm{Cl}^*+\mathrm{BCl}_3\rightarrow\mathrm{BCl}_2+\mathrm{Cl}+\mathrm{Cl}$	1×10^{-11}	[c]
$\mathrm{Cl}^*+\mathrm{BCl}_3\rightarrow\mathrm{BCl}_2^++\mathrm{Cl}+e$	1×10^{-11}	[c]
$\mathrm{Cl}_2^++\mathrm{BCl}_3\rightarrow\mathrm{BCl}_2^++\mathrm{Cl}_2$	1×10^{-10}	[c]
$\mathrm{Cl}+\mathrm{Cl}+\mathrm{Ar}\rightarrow\mathrm{Cl}_2+\mathrm{Ar}$	1.28×10^{-32}	25
$\mathrm{Cl}+\mathrm{Cl}+\mathrm{Cl}_2\rightarrow\mathrm{Cl}_2+\mathrm{Cl}_2$	5.4×10^{-32}	25

[a] Rate coefficients are calculated from electron energy distribution obtained in the EMCS. T_e is the electron temperature (eV).

[b] Energy loss due to vibrational excitation is included in the solution of Boltzmann's equation however the density of vibrationally excited species is not tracked in the model.

[c] Estimated.

[d] Estimated by analogy to BCl_3.

17 cm in height. The inductive power is supplied through a three-turn antenna coil above a 0.8 cm thick quartz window. The wafer is on an independently powered substrate 9 cm below the quartz window. For gate-stack etching, the 300 W ICP was sustained in $Ar/BCl_3/Cl_2=5/40/55$ at 5 mTorr with a flow rate of 100 SCCM (SCCM denotes cubic centimeter per minute at STP). The gas phase reaction mechanism is listed in Table I. The wafer size used in this simulation was 150 mm; however, the etching mechanisms discussed here are independent of wafer size.

The high-*k* gate stack used for the simulation, as shown in Fig. 1, consists of a 290 nm thick erodible photoresist mask, 40 nm thick BARC layer, 160 nm thick TiN, 20 nm HfO_2, 10 nm SiO_2 (to improve carrier mobility in the channel), and the Si substrate. The substrate bias voltage was varied to investigate the effect of ion energy on the selectivity of HfO_2 with respect to Si.[4,8] Extensive parameterizations were performed to determine the effects of the probabilities of polymer formation, polymer sputtering, and Si–B bond formation on selectivity. Parameterizations were also performed to determine whether the proposed mechanism is sensitive to the device layout or not. For example, the default gate-stack pitch (the full distance between the centers of gate stacks) of 200 nm was decreased to 150 nm and increased to 300 nm. The scaling laws discussed here were insensitive to those variations.

III. SURFACE REACTION MECHANISM FOR GATE-STACK ETCHING

A. Etching of HfO_2

Previous investigations of the plasma etching of metal oxides were used to develop our reaction mechanism. Sha and Chang[8] investigated the etching of high-*k* ZrO_2 in BCl_3/Cl_2 plasmas which shares many etch characteristics with HfO_2. They concluded that BCl_2^+ ions play an important role in removing O atoms from ZrO_2, as volatile B_2OCl_4, $B_3O_2Cl_5$, and $(BOCl)_3$. These processes, with the formation of a Si–B passivation layer, enabled a ZrO_2 to Si selectivity of 10 at ion energies near but above the threshold for ZrO_2 etching. They also found that in BCl_3/Cl_2 plasmas, HfO_2 and ZrO_2 etch rates are dependent on the BCl_2^+ density that is responsible for O atom removal, the Cl density which is responsible for Hf passivation to eventually remove Hf as $HfCl_n$ $(n=2,3,4)$, and on the bond strength of the metal-oxygen bond.[9] By operating with ion energies slightly above the etching threshold for the metal oxide, HfO_2 to Si selectivity can be obtained.

TaN/HfO_2 gate stacks have been etched employing $Ar/BCl_3/O_2$ plasmas to obtain high TaN/HfO_2 selectivity.[10] However with the presence of oxygen species in these plasmas, the Si–B passivation layer thought to be responsible for high HfO_2/Si selectivity is difficult to maintain. This results in a lower HfO_2/Si selectivity as compared to etching in $Ar/BCl_3/Cl_2$ plasmas. Wang and Donnelly[11] investigated etching of HfO_2 and poly-Si in BCl_3 plasmas as a function of substrate temperature and source power in a helicon reactor. BCl_2 and Cl were found to be the dominant gas phase radicals at all powers investigated, which is consistent with our findings. They found that selectivity of HfO_2 over Si was enhanced at low power and low substrate temperature. Nakamura *et al.*[12] etched HfO_2 films in BCl_3-containing plasmas employing an electron cyclotron resonance reactor without rf biasing. For $BCl_3/Cl_2=40/60$ mixtures, a HfO_2/Si selectivity of approximately 10 and an etch rate of 1000 Å/min were obtained. Our simulation results are in reasonable agreement with their findings.

When modeling plasma etching of new materials such as HfO_2, the fundamental experimental database required to develop the mechanism is often fragmentary. When both mechanisms and rates are not available, modeling and developing a reaction mechanism begin with examining the current databases for experimental results for etch rates and selectivity, material thermodynamic properties, and mechanisms and reaction probabilities for analogous processes, as well as theoretical expressions for general scaling laws. Based on these analyses, a sequence of reactions is proposed and probabilities assigned for bond breaking, adsorption, and etching reactions (that is, the mechanism is built). Extensive parametrizations and sensitivity analyses are then required to refine the mechanism to well represent the etch rates, threshold energies, and selectivities available from literature. This is done while acknowledging that there are always risks of uncertainties in building such a mechanism.

Following these procedures while benefiting from the insights provided by previous works, a mechanism was developed for etching HfO_2 in $Ar/BCl_3/Cl_2$ plasmas. In our mechanism the etching of HfO_2 incorporates two distinct steps—removal of Hf and of O. While Cl_2 plasmas can etch HfO_2 forming volatile $HfCl_n$ and ClO species as a result of Cl adsorption and ion impact, selectivity for HfO_2 with respect to Si cannot necessarily be ensured.[13] This is the fundamental motivation for using BCl_3/Cl_2 plasmas. Electron-impact dissociation of BCl_3 produces BCl_n $(n=1,2)$ species which have the ability to form volatile etch products such as B_2OCl_3, B_2OCl_4, BOCl, $(BOCl)_3$, and $B_3O_2Cl_5$. These species also have the ability to inhibit Si etching through formation of a BCl_n polymer.

In our mechanism, HfO_2 etching is initiated by the breaking of the Hf–O bonds, each having bond strength of approximately 8.3 eV. By analogy with other processes and through parametric studies, a threshold energy of 14 eV was assigned to the Hf–O bond breaking step. The first such process breaks one Hf–O bond in HfO_2, and so generates $HfO(s)$ and $O(s)$, where (s) denotes a surface resident species. A second above threshold ion can break the remaining Hf–O bond in $HfO(s)$ to produce $O(s)$ and $Hf(s)$. The exposed $Hf(s)$ sites are subsequently passivated by Cl to produce $HfCl_n(s)$ $(n=1-4)$ and ultimately a volatile etch product $HfCl_n(g)$ following ion impact. (Note that at low temperatures, $HfCl_4$ may be formed as a loosely adhered nonvolatile product that requires ion activation for removal.)

Exposed $HfO(s)$ sites are passivated by $Cl(g)$ leading to the formation of $HfOCl(s)$ and $HfOCl_2(s)$. The Hf atom in $HfOCl(s)$ and $HfOCl_2(s)$ can be removed in a single step by ion impact as volatile $HfCl_n(g)$ leaving behind $O(s)$ with a dangling bond on the surface. Although the probability is small, $Cl(g)$ can adsorb on $HfO_2(s)$ forming solids such as $HfO_2Cl(s)$ and $HfO_2Cl_2(s)$. The first Hf–O bond in these species can be broken by ion bombardment producing nonvolatile $HfOCl(s)$ and $HfOCl_2(s)$.

The full reaction mechanism for $Hf(s)$ removal is listed in Table II and, in summary, is

$$M^{+}(g) + \mathrm{HfO_2}(s) \rightarrow \mathrm{HfO}(s) + \mathrm{O}(s) + M(g), \tag{2}$$

$$M^{+}(g) + \mathrm{HfO}(s) \rightarrow \mathrm{Hf}(s) + \mathrm{O}(s) + M(g), \tag{3}$$

$$\mathrm{Cl}(g) + \mathrm{HfCl}_{n-1}(s) \rightarrow \mathrm{HfCl}_n(s) \quad (n = 1,4), \tag{4}$$

$$M^{+}(g) + \mathrm{HfCl}_x(s) \rightarrow \mathrm{HfCl}_n(g) + M(g), \tag{5}$$

$$\mathrm{Cl}(g) + \mathrm{HfO}(s) \rightarrow \mathrm{HfOCl}(s), \tag{6}$$

$$M^{+}(g) + \mathrm{HfOCl}_x(s) \rightarrow \mathrm{O}(s) + \mathrm{HfCl}_n(g) + M(g), \tag{7}$$

where $M^{+}(g)$ represents an ion.

To remove bonded oxygen on the surface, the site can adsorb $BCl_n(g)$ $(n=1,2)$ forming $OBCl_n(s)$. These complexes can then be removed by ion bombardment. The bonded oxygen can also be removed directly by $BCl_n^{+}(g)$ $(n=1,2)$ bombardment either as $B_2OCl_4(g)$ or $B_2OCl_3(g)$. A second process for removing bonded O is initiated by $BCl_n^{+}(g)$ directly striking $HfO_2(s)$ producing $OBCl_2(s)$ and $OBCl(s)$. The $OBCl(s)$ can be etched by energetic ions as volatile $BOCl(g)$ and producing $OBCl_2(s)$. The latter can be removed by the previously described mechanism. The full reaction mechanism for $O(s)$ removal is listed in Table II and in summary is

$$\mathrm{BCl}_n(g) + \mathrm{O}(s) \rightarrow \mathrm{BCl}_n\mathrm{O}(s), \tag{8}$$

$$\mathrm{BCl}_n^{+}(g) + \mathrm{HfO_2}(s) \rightarrow \mathrm{BCl}_n\mathrm{O}(s) + \mathrm{HfO}(s), \tag{9}$$

$$M^{+}(g) + \mathrm{BCl}_n\mathrm{O}(s) \rightarrow \mathrm{B}_m\mathrm{OCl}_p(g). \tag{10}$$

One of the motivations to include BCl_3 in the gas mixture is to improve the selectivity for HfO_2 with respect to Si. Formation of a BCl_n passivation layer on the Si is believed to play an important role in obtaining this selectivity by slowing the Si etch rate. The passivation layer is proposed to form in two steps. The first is forming Si–B bonds by adsorption of BCl_n to create a base layer. The second is polymer deposition by $BCl_n(g)$ on the base layer.[4] The polymerization reaction mechanism is listed in Table III, and is summarized as

$$\mathrm{BCl}_n(g) + \mathrm{Si}(s) \rightarrow \mathrm{SiBCl}_n(s), \tag{11}$$

$$\mathrm{BCl}_n(g) + \mathrm{SiCl}_m(s) \rightarrow \mathrm{SiCl}_m\mathrm{BCl}_n(s), \tag{12}$$

$$\mathrm{BCl}_n(g) + \mathrm{SiBCl}_m(s) \rightarrow \mathrm{SiBCl}_n(s) + P(s), \tag{13}$$

$$\mathrm{BCl}_n(g) + \mathrm{SiCl}_m\mathrm{BCl}_n(s) \rightarrow \mathrm{SiCl}_m\mathrm{BCl}_n(s) + P(s), \tag{14}$$

$$M^{+}(g) + P(s) \rightarrow P^{*}(s) + M(g), \tag{15}$$

$$\mathrm{BCl}_n(g) + P(s)^{*} \rightarrow P(s) + P(s), \tag{16}$$

$$M^{+}(g) + P(s) \rightarrow \mathrm{BCl_2}(g) + M(g), \tag{17}$$

where $P(s)$ is the polymer and $P^{*}(s)$ is an activated state of the polymer generated by low energy ion bombardment with enhanced deposition rates. Although not strictly stoichiometrically correct, sputtering of the polymer produces $BCl_2(g)$ which can redeposit. As such there are two competing processes—higher ion energies increase the rate of etching of the HfO_2 while also increasing the rate of sputtering of $P(s)$ on the Si which decreases selectivity.

TABLE II. Reaction mechanism for HfO_2 etching in $Ar/BCl_3/Cl_2$ plasmas [species: $M(g)$ gas phase species, $M(s)$ surface site, and M^{+} ion].

Reaction[a–c]	Probability	Footnote
HfO_2: bond breaking		
$M^{+}(g)+HfO_2(s)\rightarrow HfO(s)+O(s)+M(g)$	0.4	d
$M^{+}(g)+HfO(s)\rightarrow Hf(s)+O(s)+M(g)$	0.4	d
$Hf(s)$ passivation		
$Cl(g)+Hf(s)\rightarrow HfCl(s)$	0.2	
$Cl(g)+HfCl(s)\rightarrow HfCl_2(s)$	0.5	
$Cl(g)+HfCl_2(s)\rightarrow HfCl_3(s)$	0.2	
$Cl(g)+HfCl_3(s)\rightarrow HfCl_4(s)$	0.2	
$HfCl_x$: etching		
$M^{+}(g)+HfCl_2(s)\rightarrow HfCl_2(g)+M(g)$	0.3	d
$M^{+}(g)+HfCl_3(s)\rightarrow HfCl_3(g)+M(g)$	0.4	d
$M^{+}(g)+HfCl_4(s)\rightarrow HfCl_4(g)+M(g)$	0.9	d
HfO_n passivation		
$Cl(g)+HfO_2(s)\rightarrow HfO_2Cl(s)$	0.1	
$Cl(g)+HfO_2Cl(s)\rightarrow HfO_2Cl_2(s)$	0.06	
$Cl(g)+HfO(s)\rightarrow HfOCl(s)$	0.2	
$Cl(g)+HfOCl(s)\rightarrow HfOCl_2(s)$	0.2	
HfO_2Cl_x: bond breaking		
$M^{+}(g)+HfO_2Cl(s)\rightarrow HfOCl(s)+O(s)+M(g)$	0.4	d
$M^{+}(g)+HfO_2Cl(s)\rightarrow HfOCl(s)+O(s)+M(g)$	0.4	d
$M^{+}(g)+HfO_2Cl_2(s)\rightarrow HfOCl_2(s)+O(s)+M(g)$	0.4	d
$M^{+}(g)+HfO_2Cl(s)\rightarrow HfOCl(s)+O(s)+M(g)$	0.4	d
$HfOCl_n$: etching		
$M^{+}(g)+HfOCl(s)\rightarrow O(s)+HfCl_x(g)+M(g)$	0.2–0.4	d
$M^{+}(g)+HfOCl_2(s)\rightarrow O(s)+HfCl_x(g)+M(g)$	0.4–0.6	d
$OBCl_n$ formation		
$BCl_2^{+}(g)+HfO_2(s)\rightarrow OBCl_2(s)+HfO(s)$	0.45	d
$BCl_2^{+}(g)+HfO_2(s)\rightarrow OBCl(s)+HfO(s)+Cl(g)$	0.45	d
$BCl_2(g)+O(s)\rightarrow OBCl_2(s)$	0.2	
$BCl_2(g)+O(s)\rightarrow OBCl(s)$	0.2	
O etching		
$BCl_2^{+}(g)+OBCl_2(s)\rightarrow B_2OCl_3(g)+Cl(g)$	0.50	d
$BCl_2^{+}(g)+OBCl_2(s)\rightarrow B_2OCl_4(g)$	0.35	d
$M^{+}(g)+OBCl(s)\rightarrow BOCl(g)+M(g)$	0.45	d

[a] Unless specified, all ions neutralize on surfaces, returning as their neutral counterparts.

[b] Gas phase species have units of flux ($cm^{-2}\ s^{-1}$). Surface species have units of fractional coverage.

[c] In reactions with no chemical change, the gas species are reflected off the surface. These reactions are not shown.

[d] See Eq. (1). $E_r=100$ eV and $E_t=10$ eV, probability is at E_r.

B. TiN etching

$TiN(s)$ etching begins with ion bombardment to break the Ti–N bond and liberate N atoms. The $Ti(s)$ site then adsorbs

TABLE III. Si–B bond formation and polymerization reactions [species: $M(g)$ gas phase species, $M(s)$ surface site, and M^+ ion].

Reaction[a–c]	Probability	Footnote
Si–B bond formation		
$BCl_n(g)+Si(s)\rightarrow SiBCl_n(s)$, $n=1,2$	0.4	
$BCl_n(g)+SiCl(s)\rightarrow SiClBCl_n(s)$, $n=1,2$	0.4	
$BCl_n(g)+SiCl_2(s)\rightarrow SiCl_2BCl_n(s)$, $n=1,2$	0.4	
$BCl_n(g)+SiCl_3(s)\rightarrow SiCl_3BCl_n(s)$, $n=1,2$	0.4	
Polymer formation on SiBCl sites		
$BCl_n(g)+SiBCl_n(s)\rightarrow SiBCl_n(s)+P_1(s)$, $n=1,2$	0.7	
$BCl_n(g)+SiClBCl_n(s)\rightarrow SiClBCl_n(s)+P_1(s)$, $n=1,2$	0.7	
$BCl_n(g)+SiCl_2BCl_n(s)\rightarrow SiCl_2BCl_n(s)+P_1(s)$, $n=1,2$	0.7	
$BCl_n(g)+SiCl_3BCl_n(s)\rightarrow SiCl_3BCl_n(s)+P_1(s)$, $n=1,2$	0.7	
Polymer formation on activated sites		
$BCl_2(g)+P_1{}^*(s)\rightarrow P_1(s)+P_2(s)$	0.70	
$BCl(g)+P_1{}^*(s)\rightarrow P_1(s)+P_2(s)$	0.70	
$BCl_2(g)+P_2{}^*(s)\rightarrow P_2(s)+P_2(s)$	0.70	
$BCl_2(g)+P_2{}^*(s)\rightarrow P_2(s)+P_2(s)$	0.70	
Polymer activation and sputtering		
$M^+(g)+P_1(s)\rightarrow P_1{}^*(s)+M(g)$	0.10	d
$M^+(g)+P_2(s)\rightarrow P_2{}^*(s)+M(g)$	0.15	d
$M^+(g)+P_1{}^*(s)\rightarrow BCl_2(g)+M(g)$	0.10	e
$M^+(g)+P_2{}^*(s)\rightarrow BCl_2(g)+M(g)$	0.15	e

[a] Unless specified, all ions neutralize on surfaces, returning as their neutral counterparts.
[b] Gas phase species have units of flux ($cm^{-2}\ s^{-1}$). Surface species have units of fractional coverage.
[c] In reactions with no chemical change, the gas species are reflected off the surface. These reactions are not shown.
[d] $p(E)=\max[p_0(1-E/E_c),0]$, where E_c is the cutoff energy for polymer activation. $p_0=0.1$ and $E_c=45$ eV.
[e] See Eq. (1). $E_r=140$ eV and $E_t=45$ eV.

$Cl(g)$ leading to the formation of $TiCl_n(s)$ $(n=1,2,3)$. Ion bombardment removes these compounds as $TiCl_n(g)$.[26] $TiN(s)$ can itself adsorb $Cl(g)$ to produce $TiNCl(s)$ followed by energetic ion bombardment containing Cl to directly remove Ti from $TiNCl(s)$ as volatile $TiCl_n(g)$. In an integrated gate-stack etching process, the PR may be trimmed and BARC removed in plasmas producing O atoms. When the TiN surface is exposed to both energetic ions and O atoms, Ti–N bond breaking followed by O atom adsorption can form nonvolatile $TiO(s)$. Then, when etching the gate stack in $Ar/BCl_3/Cl_2$ plasmas, $TiO(s)$ adsorbs $Cl(g)$ forming $TiOCl_n(s)$ $(n=1,2)$. These oxichlorides can then be removed as volatile $TiOCl_n(g)$ $(n=1,2)$ by ion bombardment. The reaction mechanism for $TiN(s)$ etching is listed in Table IV and is summarized as

$$M^+(g)+TiN(s)\rightarrow Ti(s)+N(g)+M^+(g), \tag{18}$$

$$Cl(g)+TiCl_{n-1}(s)\rightarrow TiCl_n(s)\quad (n=1,3), \tag{19}$$

$$M^+(g)+TiCl_n(s)\rightarrow TiCl_n(g)+M(g)\quad (n=1-3), \tag{20}$$

$$Cl(g)+TiCl_3(s)\rightarrow TiCl_4(g). \tag{21}$$

IV. PHOTORESIST TRIMMING, BARC ETCHING, AND PR EROSION

As gate length shrinks below 50 nm, 193 nm lithography is challenged to directly define the features.[27–29] Consequently, when the width of the PR line after lithography is larger than the desired dimensions, trimming of the PR is often employed. For organically based PR, controlled exposure to an O_2 containing plasma will etch back the PR to a smaller dimension. Such plasmas may also reduce the sidewall roughness of the PR. For example, Hwang *et al.*[26] investigated trimming of PR and etching of BARC in an integrated step employing CF_4/O_2 plasmas. The oxygen provided a high PR removal rate while the polymerizing CF_4 maintained a vertical PR/BARC profile after trimming.[27] Although the trim rate is higher for CF_4/O_2 plasmas compared to Cl_2/O_2 and HBr/O_2 plasmas, the amount of oxygen found on the PR sidewall after trimming is higher.[28] In spite of its slow trim rate, precise control of the CD during trimming has been obtained using Cl_2/O_2 plasmas.[28,29] It has also been shown that Ar/O_2 plasmas generate a vertical and uniform PR profile with a high PR removal rate.[30]

To simulate the full gate-stack etching process, we included a PR-trim step prior to exposure to the $Ar/BCl_3/Cl_2$ plasma. The PR-trim step was performed in an Ar/O_2

TABLE IV. Reaction mechanism for TiN etching and PR/BARC sputtering in $Ar/BCl_3/Cl_2$ plasmas [species: $M(g)$ gas phase species, $M(s)$ surface site, and M^+ ion].

Reaction[a–c]	Probability	Footnote
Bond breaking		
$M^+(g)+TiN(s)\rightarrow Ti(s)+N(g)+M(g)$	0.51	d
Passivation		
$Cl(g)+Ti(s)\rightarrow TiCl(s)$	0.89	
$Cl(g)+TiCl(s)\rightarrow TiCl_2(s)$	0.65	
$Cl(g)+TiCl_2(s)\rightarrow TiCl_3(s)$	0.65	
$Cl(g)+TiN(s)\rightarrow TiNCl(s)$	0.51	
$O(g)+Ti(s)\rightarrow TiO(s)$	0.51	
$Cl(g)+TiO(s)\rightarrow TiOCl(s)$	0.60	
$Cl(g)+TiOCl(s)\rightarrow TiOCl_2(s)$	0.60	
Etching		
$Cl(g)+TiCl_3(s)\rightarrow TiCl_4(g)$	0.02	
$M^+(g)+TiCl(s)\rightarrow TiCl(g)+M(g)$	0.35	d
$M^+(g)+TiCl_2(s)\rightarrow TiCl_2(g)+M(g)$	0.45	d
$M^+(g)+TiCl_3(s)\rightarrow TiCl_3(g)+M(g)$	0.65	d
$M^+(g)+TiNCl(s)\rightarrow TiCl_x(g)+M(g)$	0.35	d
$M^+(g)+TiOCl(s)\rightarrow TiOCl(g)+M(g)$	0.60	d
$M^+(g)+TiOCl_2(s)\rightarrow TiOCl_2(g)+M(g)$	0.60	d
PR and BARC: sputtering and redeposition		
$M^+(g)+PR(s)\rightarrow PR(g)+M(g)$	0.02	d
$M^+(g)+BARC(s)\rightarrow BARC(g)+M(g)$	0.05	d
$PR(g)+M(s)\rightarrow PR(s)+M(s)$	0.01	e
$BARC(g)+M(s)\rightarrow BARC(s)+M(s)$	0.01	e

[a] Unless specified, all ions neutralize on surfaces, returning as their neutral counterparts.

[b] Gas phase species have units of flux ($cm^{-2}\ s^{-1}$). Surface species have units of fractional coverage.

[c] In reactions with no chemical change, the gas species are reflected off the surface. These reactions are not shown.

[d] See Eq. (1)

$E_r=100$ eV and $E_t=10$ eV, probability is at E_r.

[e] PR(g) and BARC(g) can redeposit on all surfaces. The redeposited material as the same characteristics as the original PR and BARC.

TABLE V. Reaction mechanism for PR trimming and BARC etching [species: $M(g)$ gas phase species, $M(s)$ surface site, and M^+ ion].

Reaction[a–c]	Probability	Footnote
PR sputtering		
$M^+(g)+PR(s)\rightarrow PR(g)+M(g)$	0.020	d
PR etching		
$O(g)+PR(s)\rightarrow COH(g)$	0.010	
$O^+(g)+PR(s)\rightarrow COH(g)$	0.010	
$O_2{}^+(g)+PR(s)\rightarrow COH(g)$	0.010	
BARC sputtering		
$M^+(g)+BARC(s)\rightarrow BARC(g)+M(g)$	0.050	d
BARC etching		
$O(g)+BARC(s)\rightarrow COH(g)$	0.015	
$O^+(g)+BARC(s)\rightarrow COH(g)$	0.015	
$O_2{}^+(g)+BARC(s)\rightarrow COH(g)$	0.015	
Redeposition		
$PR(g)+M(s)\rightarrow PR(s)+M(s)$	0.01	e
$BARC(g)+M(s)\rightarrow BARC(s)+M(s)$	0.01	e

[a] Unless specified, all ions neutralize on surfaces, returning as their neutral counterparts.

[b] Gas phase species have units of flux ($cm^{-2}\ s^{-1}$). Surface species have units of fractional coverage.

[c] In reactions with no chemical change, the gas species are reflected off the surface. These reactions are not shown.

[d] See Eq. (1). $E_r=100$ eV and $E_t=10$ eV.

[e] PR(g) and BARC(g) can redeposit on all surfaces. The redeposited material as the same characteristics as the original PR and BARC.

plasma which also served to remove the BARC layer. The intent of the trim process was to reduce the initial photoresist having a height of 290 nm and a width of 58 nm to a width of 32 nm.

As both BARC and PR are primarily hydrocarbons, they can be chemically etched by plasma produced oxygen species such as $O(g)$, $O^+(g)$, and $O_2{}^+(g)$ and chemically sputtered by the ions. The reaction mechanism for Ar/O_2 plasma etching of the organic PR and BARC is listed in Table V, and is summarized as follows [note that $COH(g)$ is a *generic* PR and BARC etch product which can redeposit as a PR or BARC species but is otherwise unreactive in the plasma]:

$$M^+(g)+PR(s)\rightarrow PR(g)+M(g), \tag{22}$$

$$M^+(g)+BARC(s)\rightarrow BARC(g)+M(g), \tag{23}$$

$$O(g)+PR(s)\rightarrow COH(g), \tag{24}$$

$$O(g)+BARC(s)\rightarrow COH(g), \tag{25}$$

$$O_n{}^+(g)+PR(s)\rightarrow COH(g), \tag{26}$$

$$O_n{}^+(g)+BARC(s)\rightarrow COH(g). \tag{27}$$

If the BARC is completely cleared during the PR trim, ions in the Ar/O_2 plasma can break Ti–N bonds to produce $Ti(s)$ sites which then adsorb $O(g)$ to produce $TiO(s)$. During the gate-stack etch in $Ar/BCl_3/Cl_2$ plasmas, the $TiO(s)$ sites can further adsorb $Cl(g)$ to produce $TiOCl(s)$ and $TiOCl_2(s)$. Ions in the $Ar/BCl_3/Cl_2$ plasma remove these species as volatile $TiOCl(g)$ and $TiOCl_2(g)$. A summary of the reactions for $TiO(s)$ and $TiOCl_n(s)$ $(n=1,2)$ formation and removal are (see Table IV)

$$M^+(g)+TiN(s)\rightarrow Ti(s)+N(g)+M(g), \tag{28}$$

$$O(g)+Ti(s)\rightarrow TiO(s), \tag{29}$$

$$Cl(g)+TiO(s)\rightarrow TiOCl(s), \tag{30}$$

$$Cl(g)+TiOCl(s)\rightarrow TiOCl_2(s), \tag{31}$$

$$M^+(g)+TiOCl_n(s)\rightarrow TiOCl_n(g)+M(g), \quad n=1,2. \tag{32}$$

There will be a tradeoff between fully removing the BARC and exposing the TiN to the oxygen plasma and leaving a thin BARC later that must be removed during the gate-stack etch.

The process conditions for the PR trimming and BARC etching were 5 mTorr, $Ar/O_2=5/95$ gas mixture with a flow rate of 100 SCCM. The coil delivered 300 W at 10 MHz. A bias of 18 V was applied to the substrate. Probabilities for BARC and PR etching were varied to determine the values required to maintain an acceptable CD while also trimming the PR. It was found that when the BARC etch rate is 1.5 times higher than the PR etch rate, these goals are met. For example, post-trim gate-stack profiles with relative etching probabilities between the BARC and PR of 1.5, 1.0, and 0.5 are shown in Fig. 3. With the BARC etch rate 1.5 times that of the PR, a good CD was obtained; however a small amount of BARC was left on the TiN which produced micromasking during the etch steps. When the PR and BARC etch rates are equal, the PR width shrank below 25 nm and a 5–10 nm layer of BARC micromasking was left on the TiN. Leaving this layer would require more time in the gate-stack etch step to clear the BARC due to the absence of O species in the $Ar/BCl_3/Cl_2$ plasma. To totally clear the BARC during the trim would produce an unacceptably narrow PR.

V. PLASMA AND HFO_2 ETCH PROPERTIES

The process conditions for the gate-stack etch were a 5 mTorr $Ar/BCl_3/Cl_2=5/40/55$ gas mixture with a flow rate of 100 SCCM. The coil delivered 300 W at 10 MHz. The amplitude of the 13.56 MHz rf bias on the substrate was varied. The total ion density was $3.2\times10^{11}\ cm^{-3}$. BCl_2^+ has the highest density ($1.6\times10^{11}\ cm^{-3}$) followed by Cl^+ ($1.0\times10^{11}\ cm^{-3}$). Cl is the radical with the largest density ($1.0\times10^{14}\ cm^{-3}$) followed by BCl_2 ($1.3\times10^{13}\ cm^{-3}$) (see Fig. 2). Fluxes of the major ions and neutral radicals to the substrate are shown in Fig. 4 for the base case with a 32 V substrate bias. The dominant radical fluxes are Cl ($1\times10^{18}\ cm^{-2}\ s^{-1}$) and BCl_2 ($7.5\times10^{16}\ cm^{-3}\ s^{-1}$). Cl is produced by both electron impact dissociation of Cl_2 and BCl_3, the latter yielding BCl_2 and Cl. Electron-impact ionization of BCl_3 dominantly produces BCl_2^+ and Cl. The major ion fluxes are BCl_2^+ ($8\times10^{15}\ cm^{-2}\ s^{-1}$), Cl^+ ($4\times10^{15}\ cm^{-2}\ s^{-1}$), Cl_2^+ ($4\times10^{14}\ cm^{-2}\ s^{-1}$), and Ar^+ ($4\times10^{13}\ cm^{-2}\ s^{-1}$). The low flux of Ar^+ results from the low mole fraction of Ar but also from rapid charge exchange reactions to other species. With a 32 V bias, the average energy for all ions incident on the substrate is near 30 eV with an angular spread from the vertical of <15°, as shown by the IEADs in Fig. 5.

A. HfO_2 etch rate versus bias voltage

Bias voltage affects the properties of the gate-stack etch through rate, profile, and selectivity of HfO_2 to Si. The postetch gate-stack profiles for biases of 32, 60, and 100 V are shown in Fig. 6(a) for equal etch times corresponding to the time when the 32 V bias removes the SiO_2 layer. Etch rate and selectivity as a function of bias voltage are shown in Fig. 6(b). The etch rate of HfO_2 has a threshold bias of 27 V increasing from 100 Å/min at 32 V to 650 Å/min at 200 V. The increase in etch rate slows above 100 V as the rates of increase in ion activated reaction probabilities begin to saturate. The increase in etch rate comes at the expense of selectivity. The selectivity is as large as 12 at a bias of 32 V, decreasing monotonically to 2 for a bias of 200 V. The decrease in selectivity is largely a consequence of the removal of polymer on the Si by sputtering.

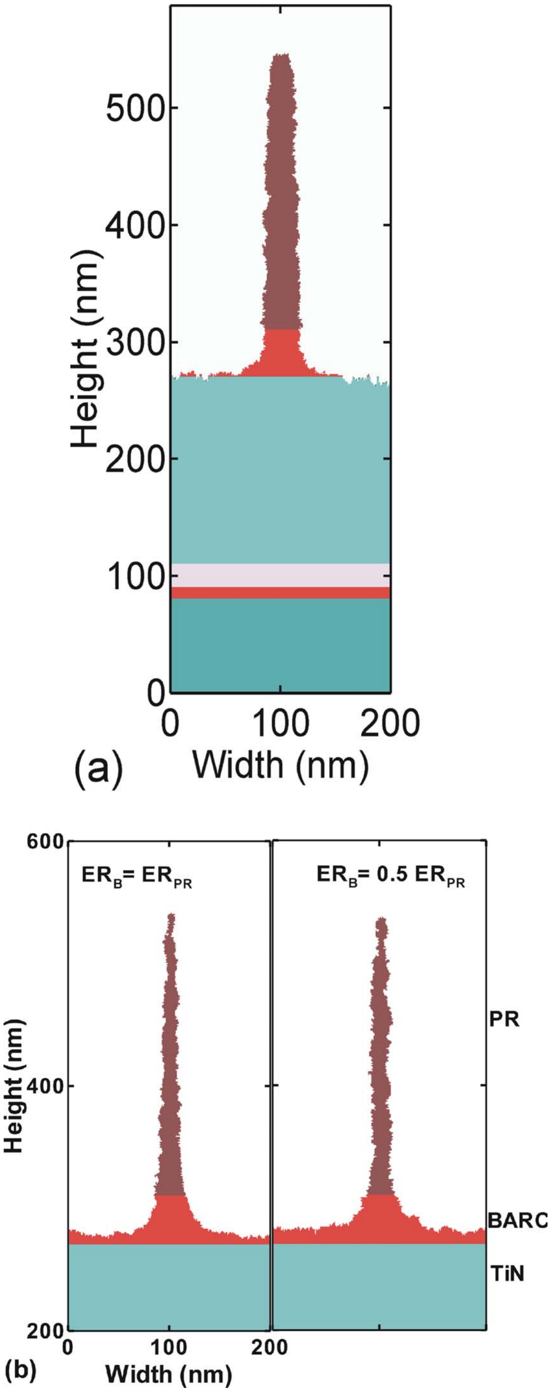

FIG. 3. (Color online) Gate stack after PR trimming and BARC etching in Ar/O_2 plasmas. (a) Optimized post-PR-trim profile with BARC to PR etching ratio of 1.5. (b) Post-PR-trim profiles while varying PR and BARC etching probabilities. The ratios of etching of BARC to PR are 1.5, 1, and 0.5 respectively.

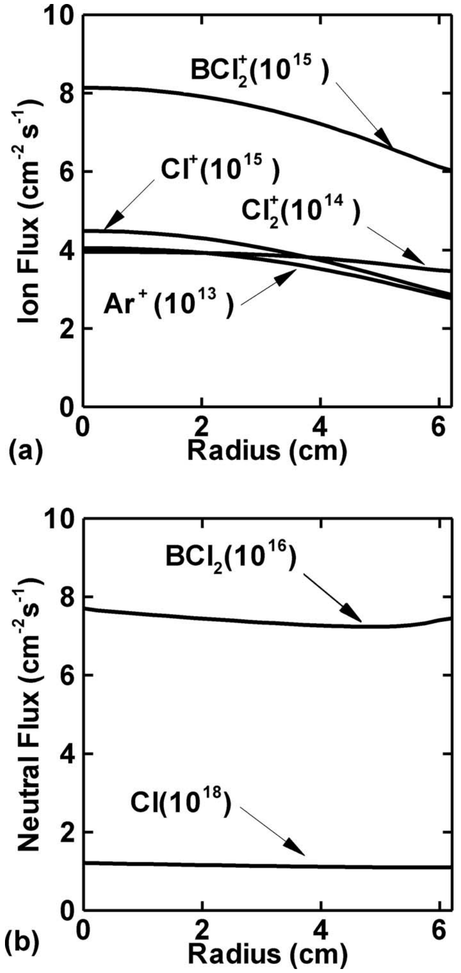

FIG. 4. Fluxes to the wafer as a function of radius ($Ar/BCl_3/Cl_2$ $=5/40/55$, 300 W ICP, 5 mTorr, and 100 SCCM). (a) Ion fluxes and (b) neutral fluxes. The scaling for fluxes are indicated in the figure. Cl is the major neutral radical flux and BCl_2^+ is the dominant ion.

Our predicted threshold of 27 V for HfO_2 etching is in agreement with the experimentally measured threshold of 28 V.[9,13] The predicted high selectivity near the etching threshold is corroborated by experimental results where highly selective etching of HfO_2 layer over Si was achieved by control of the substrate bias.[4,13] The predicted decrease in selectivity as a function of increasing bias is also in general agreement with experiment, although our decrease in selectivity is more gradual.[13] Predicted HfO_2 etch rates for biases of 32–200 V bias are also in general agreement with experiment, with differences attributable to differences in the total fluxes of reactants in the reactors used by different researchers.[4,12,13]

The increase in bias voltage also produces undercutting of the TiN. In spite of a narrowing of the IEAD with increasing bias, there is still sufficient width to produce some lateral etching due to the open field on both sides of the feature. This is an affect that would not be as apparent in trench or via etching where at higher aspect ratios, the ions at broader angles are shadowed.

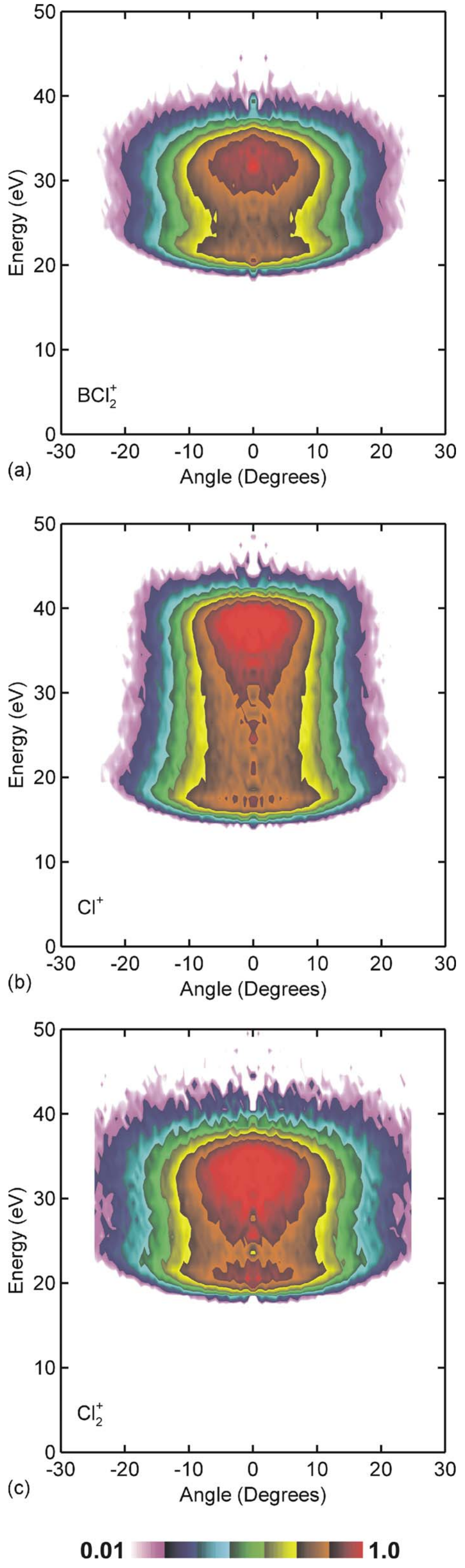

FIG. 5. (Color online) IEADs to the wafer. (a) BCl_2^+, (b) Cl^+, and (c) Cl_2^+. Plasma conditions are $Ar/BCl_3/Cl_2=5/40/55$, 300 W ICP, 5 mTorr, 100 SCCM, and a bias of 18 V.

Gate-stack profiles at the time when the SiO_2 layer is cleared for each bias are shown in Fig. 7(a) for 32, 60, and 100 V. Using a qualitative assessment of maintaining CD (that is, a vertical profile) while minimizing Si damage, the

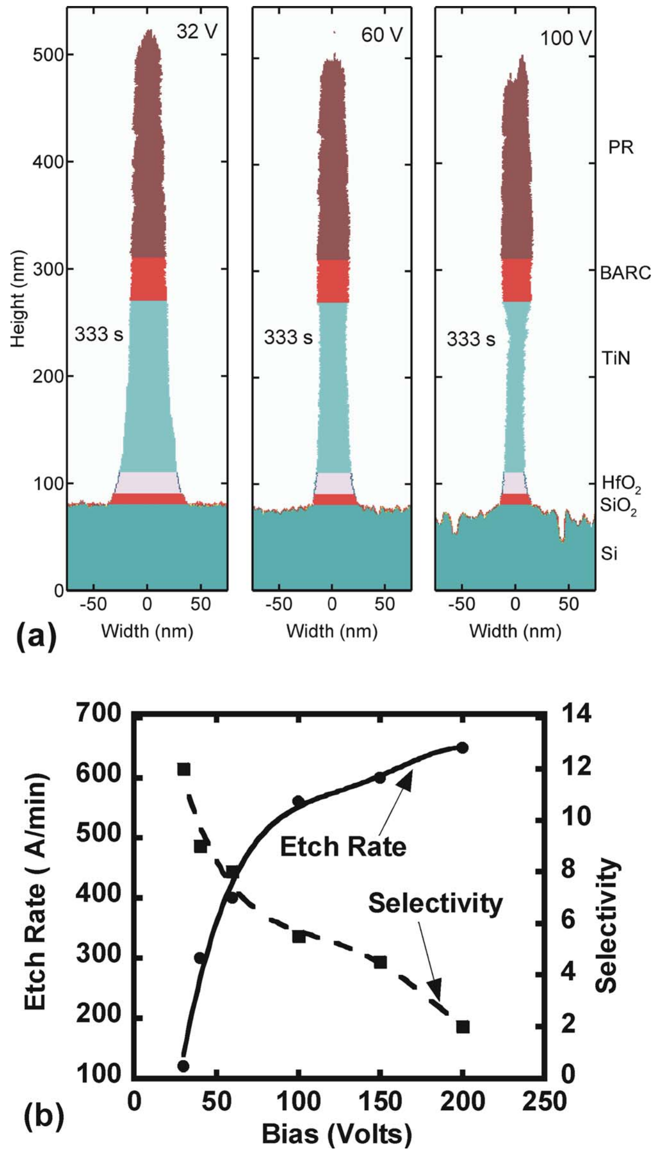

FIG. 6. (Color online) Profiles and rates for gate-stack etching (Ar/BCl$_3$/Cl$_2$=5/40/55, 300 W ICP, 5 mTorr, and 100 SCCM). (a) HfO$_2$ gate-stack profiles for biases of 32, 60, and 100 V for equal etch times corresponding to when the SiO$_2$ layer is cleared with a 32 V bias. (b) HfO$_2$ etch rate and selectivity as a function of bias voltage. Damage to Si occurs for biases significantly above 30 V.

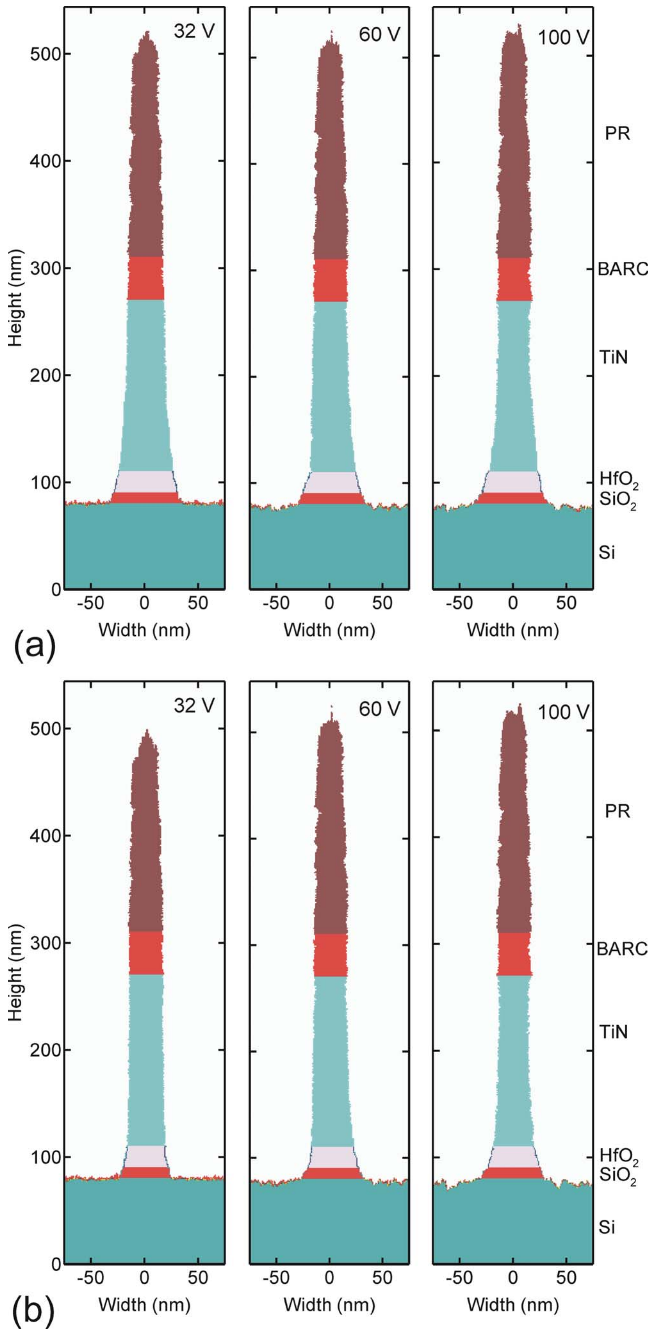

FIG. 7. (Color online) Postetch gate-stack profiles for 32, 60, and 100 V. (a) For times when the SiO$_2$ is cleared and (b) optimized profiles with respect to overetch time.

best profiles obtained for 32, 60, and 100 V biases as a function of overetch time are shown in Fig. 7(b). The high HfO$_2$/Si selectivity afforded by the 32 V bias allows a sufficient overetch to produce a largely uniform gate-stack width. There is a little damage to the Si substrate although there is a small narrowing of the TiN. The lower selectivity obtained with a 60 V bias produced some damage to the Si layer while the gate stack has less narrowing. This damage is, in part, due to the initial micromasking of the TiN by the BARC and TiO, which ultimately produces different clearing times to the Si at different locations. Those TiN sites that are micromasked have a delayed start to etching corresponding to when the masking material (BARC or TiO) is removed. Although the BARC and TiO that produce micromasking are more rapidly removed with the higher bias, thereby reducing the negative aspects of micromasking, the etch rates of the TiN, HfO$_2$, and SiO$_2$ are also more rapid with increasing bias. This leads to overetching at random sites on the Si that were not micromasked. Further etching to remove the tapering in the gate stack then produces more Si damage. These trends are intensified with the 100 V bias as both the HfO$_2$/Si selectivity decreases and the CD worsens (narrowing of the gate stack.).

Both an acceptable CD and HfO$_2$/Si selectivity were obtained with a 32 V bias where the TiN and HfO$_2$ had a nearly consistent width of 32 nm. A slight tapering of the TiN and HfO_2 occurred for the 60 V bias with a small amount of damage to the Si. The profile could not be optimized for both width and lack of damage to the Si at 100 V. For example, the TiN narrowed to a width of below 25 nm, with there being significant erosion of the Si substrate.

As discussed above, depending on the ratio of the PR to BARC etch rates during the PR-trim step, there may be micromasking on the TiN at the end of the trim step due to incomplete removal of the BARC. In practice, the remaining BARC layer is often removed with an intermediate plasma etching step prior to the gate-stack etch to eliminate the possibility of micromasking. In the absence of the BARC removal step, the micromasking material is dominantly removed by sputtering reactions during the gate-stack etch, which also serves to further erode the PR. For example, while clearing the micromasking layer and etching the gate stack in the base case, the PR width was further reduced by a few nanometers. Sites underneath the micromasking etch more slowly due to the prior need to remove the BARC by sputtering. For example, time sequences of the gate-stack profile with biases of 32 and 100 V are shown in Fig. 8 with BARC micromasking remaining from the PR trim. If the selectivity of HfO_2/Si is high enough, as with the 32 V bias, the different clearing times of the TiN and HfO_2 laterally across the feature due to micromasking are not detrimental to either the final CD or selectivity. For low selectivity conditions, as with the 100 V bias, the micromasking is problematic as the overetch results in local sites on the Si being damaged.

A quantitative measure of CD is the slope of the gate-stack profile where 90° would indicate a vertical profile. The slope of the gate-stack profile is shown in Fig. 9 for different biases as a function of overetch time. The beginning of the overetch is when the SiO_2 on top of the Si substrate is cleared. The asymptotic slope at long overetch is 80°–90° with higher biases both achieving a slope nearer the vertical and achieving that slope with shorter overetch times. These more optimum slopes are obtained at the expense of poor selectivity.

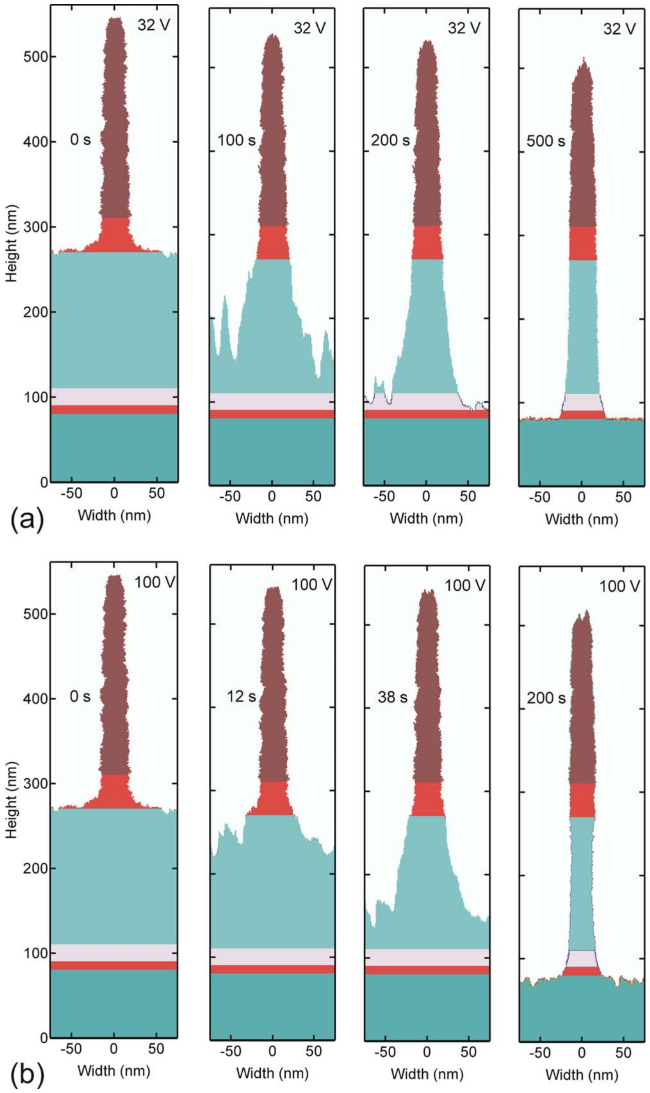

Fig. 8. (Color online) Time sequences for gate-stack profile evolution showing the effect of BARC micromasking on damage to the Si substrate with low and high bias voltages. (a) With a 32 V bias micromasking does not cause significant damage to the Si during the overetch due to the high selectivity. (b) With a 100 V bias the more rapid exposure of Si sites not micromasked produces damage.

B. Selectivity: Si–B bond formation

The selectivity of HfO_2 to Si depends on the formation and persistence of the BCl_n polymer layer. To determine the sensitivity of selectivity to rates of Si–B bond formation, polymer deposition, and polymer sputtering, the probabilities for these processes were parametrized in the model.

Selectivity while varying the probability of the Si–B bond formation that initiates the deposition of polymer is shown in Fig. 10(a) for different bias voltages. The corresponding gate-stack profiles are shown in Fig. 11(a). In the absence of Si–B bond formation, the polymer does not deposit and so the selectivity is based only on the intrinsic etch rates of the HfO_2 and the Si, which for the base case conditions are nearly equal. As the probability for Si–B bond formation increases from 0 to 0.4, the rate of etching of Si slows and the selectivity improves to 10 for a bias of 32 V. At this probability, the majority of the available sites are passivated and covered by BCl_n polymer. Although selectivity increases with increasing bond formation probability for all biases, as the bias voltage and sputtering rates increase, the residence time of Si–B bonding decreases and so the rate of polymer formation also decreases. The end result is a decrease in selectivity with bias voltage. For example, for a bias of 100 V, only 45% of the Si sites are, on the average, passivated.

The gate-stack profile prior to reaching the Si layer is essentially independent of the Si–B bond formation probability for a given etch time. The consequences of Si–B bonding are only felt once the SiO_2 layer is cleared. With a low Si–B bond formation probability, sites on the Si are periodically exposed to the plasma, producing roughness and damage, as shown in Fig. 11(a). Increasing the bond formation probabil-

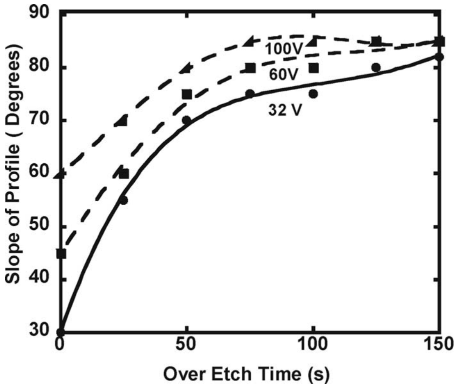

FIG. 9. Slopes of the gate-stack profile for different bias voltages as a function of overetch time. A vertical profile corresponds to 90°. Higher bias voltages achieve more vertical profiles with less overetch but at the cost of selectivity.

ity ensures that these sites are nearly continuously passivated, thereby reducing the propensity for damage.

C. Selectivity: Polymer deposition

Provided that Si–B bonds are present, $BCl_n(g)$ species adsorb on top of Si–B compounds to form BCl_n polymers.[4] Selectivity as a function of polymer deposition probability and interface properties for different bias voltages are shown in Figs. 10(b) and 11(b). As the probability for polymer deposition is increased from 0 to 0.5, the selectivity improves from 3 to 10 for a bias of 32 V. The selectivity is almost constant at probabilities higher than 0.5. Selectivity is above 2 for all biases even in the absence of polymer formation as the Si etch rate is slowed by the base layer of Si–B bonding. As the bias voltage increases, the rates of sputtering of the polymer and Si–B bond breaking increase resulting in a lower selectivity. Increasing the bias to 100 V reduces selectivity by nearly half at all deposition probabilities. Again, the gate-stack profile is independent of the polymer formation rate although the roughness and damage to the Si layer increases with increasing bias, as shown in Fig. 11(b).

D. Selectivity: Polymer sputtering

As the polymer is deposited, it is also necessary that the polymer be sustained in order to obtain high selectivity. Higher polymer sputtering rates produce thinner polymer layers and so results in lower selectivity. For example, selectivity as a function of the polymer sputtering probability (this is the probability at the reference energy of 140 eV) is shown in Fig. 10(c) for biases of 40, 100, and 150 V bias. Gate-stack profiles for different polymer sputtering probabilities are shown in Fig. 12. Selectivity decreases with increasing polymer sputtering probability while the Si roughness and damage increase.

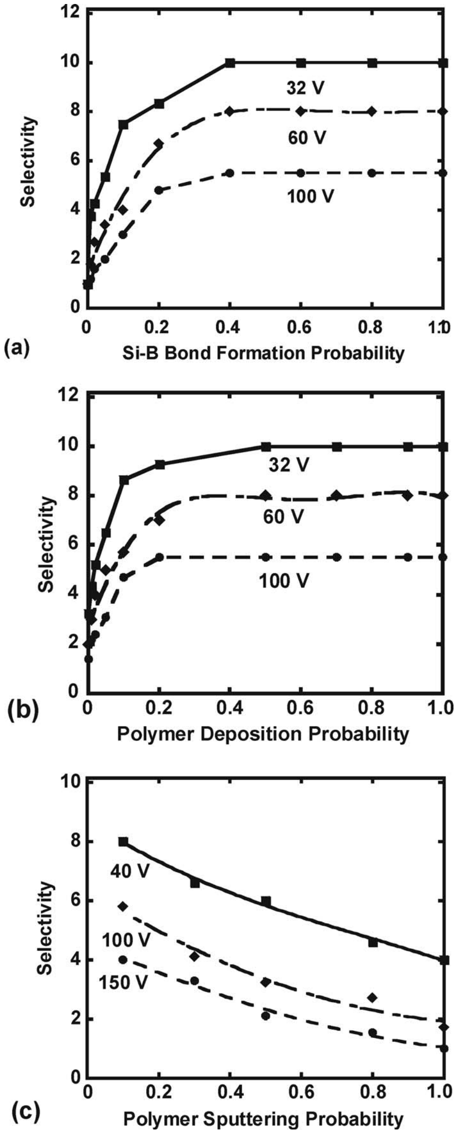

FIG. 10. HfO_2/Si selectivity for different bias voltages as a function of the probabilities for (a) Si–B bond formation, (b) polymer deposition, and (c) polymer sputtering. ($Ar/BCl_3/Cl_2=5/40/55$, 300 W ICP, 5 mTorr, and 100 SCCM).

VI. CONCLUDING REMARKS

$PR/BARC/TiN/SiO_2/Si$ gate-stack etching employing $Ar/BCl_3/Cl_2$ plasmas preceded by an Ar/O_2 plasma PR trim and BARC removal was computationally investigated. HfO_2 etching likely requires breaking of Hf–O bonds and separate removal of Hf(s) and O(s) atoms by Cl(g) adsorption and ion assisted etching. Etching of TiN likely includes breaking of Ti–N bonds and chlorination of Ti(s) to be removed as $TiCl_n(g)$. The model confirms that HfO_2/Si selectivity can be achieved by deposition of a BCl_n polymer on the Si, preceded by Si–B bond formation. With low biases, selective etching of HfO_2 with respect to Si can be achieved while minimizing undercutting of the TiN gate due to the persistence of the polymer layer. A significant overetch, however, is required to achieve the optimum etch profile (that is, closest to 90°). While higher bias voltages require less time to achieve a profile slope close to 90°, this is achieved at the cost of selectivity. The role of Si–B bond formation and growth of BCl_n polymer were parametrically investigated.

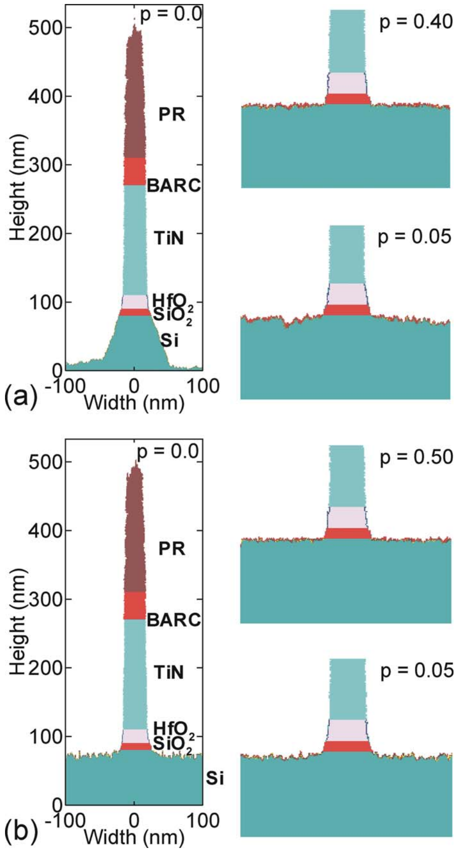

FIG. 11. (Color online) Postetch gate-stack profiles while varying Si–B formation and polymer formation probabilities. (a) Profiles for Si–B bond formation probabilities of 0.0, 0.05, and 0.4. (b) Profiles for polymer formation probabilities of 0.0, 0.05, and 0.4. For both cases selectivity improves with probability until the Si sites are nearly uniformly passivated. ($Ar/BCl_3/Cl_2=5/40/55$, 300 W ICP, 5 mTorr, and 100 SCCM).

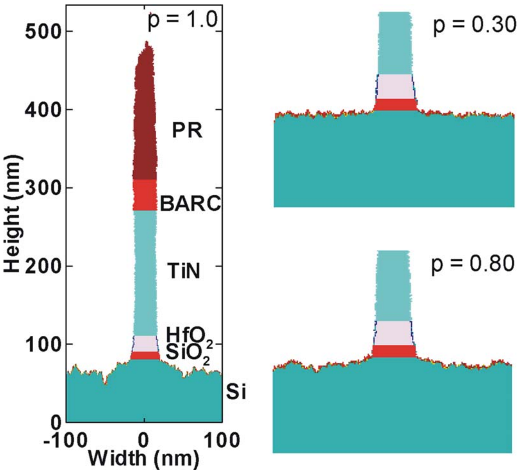

FIG. 12. (Color online) Postetch gate-stack profiles for polymer sputtering probabilities of 0.3, 0.8, and 1.0 ($Ar/BCl_3/Cl_2=5/40/55$, 300 W ICP, 5 mTorr, and 100 SCCM).

We found that both Si–B bond formation and polymer deposition are necessary to achieve high selectivity although some nominal selectivity is afforded by the Si–B bonding.

Optimizing the PR trim prior to the gate-stack etch involves a tradeoff between maintaining the CD of the PR and total removal of the BARC. This tradeoff results from the PR and BARC both typically being organics having similar etch rates in oxygen containing plasmas. Parameterization showed that a BARC etch rate 1.5 times higher than that of the PR provides the best post-trim profile. A thin layer of BARC left on the TiN produces micromasking which must first be removed during the gate-stack etch. At low bias voltages, this micromasking was not necessarily detrimental to the final gate-stack profile and did not significantly contribute to damaging the Si due to the need to overetch. These trends resulted from the high HfO_2/Si selectivity at low bias voltages that protects the Si substrate sites during even a long overetch.

Although the reaction mechanism we developed does reproduce experimental trends, there are uncertainties in both the sequence of reactions and in reaction probabilities. For example, our studies have shown the range of probabilities for important processes, such as for sputtering and polymer deposition, over which predicted etch rates and selectivity are most sensitive. The test of the mechanism is whether it provides accurate predictions for process conditions considerably different from that used to help create the mechanisms. As such refinement of the mechanism will benefit from further comparisons to experiments.

ACKNOWLEDGMENT

This work was supported by the Semiconductor Research Corporation.

[1] R. Chau *et al.*, Microelectron. Eng. **80**, 1 (2005).
[2] B. H. Lee, L. Kang, R. Nieh, W.-J. Qi, and J. C. Lee, Appl. Phys. Lett. **76**, 1926 (2000).
[3] R. Chau, S. Datta, M. Doczy, B. Doyle, J. Kavalieros, and M. Metz, IEEE Electron Device Lett. **25**, 408 (2004).
[4] E. Sungauer, E. Pargon, X. Mellhaoui, R. Ramos, G. Cunge, L. Valier, O. Joubert, and T. Lill, J. Vac. Sci. Technol. B **25**, 1640 (2007).
[5] M. J. Kushner, J. Appl. Phys. **94**, 1436 (2003).
[6] C. F. Abrams and D. B. Graves, J. Appl. Phys. **86**, 2263 (1999).
[7] A. Agarwal and M. J. Kushner, J. Vac. Sci. Technol. A **27**, 37 (2009).
[8] L. Sha and J. P. Chang, J. Vac. Sci. Technol. A **21**, 1915 (2003).
[9] L. Sha and J. P. Chang, J. Vac. Sci. Technol. A **22**, 88 (2004).
[10] M. H. Shin, M. S. Park, N.-E. Lee, J. Kim, C. Y. Kim, and J. Anh, J. Vac. Sci. Technol. A **24**, 1373 (2006).
[11] C. Wang and V. M. Donnelly, J. Vac. Sci. Technol. A **26**, 597 (2008).
[12] K. Nakamura, D. Hamada, Y. Ueda, K. Eriguchi, and K. Ono, Appl. Phys. Exp. **2**, 016503 (2009).
[13] L. Sha, R. Puthenkovilakam, Y.-S. Lin, and J. P. Chang, J. Vac. Sci. Technol. B **21**, 2420 (2003).
[14] M. Hayashi, Nagoya Institute of Technology Technical Report No. IPPJ-AM-19, 1981.
[15] K. Tachibana, Phys. Rev. A **34**, 1007 (1986).
[16] D. Rapp and P. Englander-Golden, J. Chem. Phys. **43**, 1464 (1965).
[17] R. H. McFarland and J. Kinney, Phys. Rev. **137**, A1058 (1965).
[18] I. P. Zapesochnyi and L. L. Shimon, Opt. Spectrosc. **11**, 155 (1966).
[19] G. L. Rogoff, J. M. Kramer, and R. B. Piejak, IEEE Trans. Plasma Sci. **14**, 103 (1986).
[20] R. Nagpal and A. Garscadden, Appl. Phys. Lett. **64**, 1626 (1994).
[21] J. Marriott and J. D. Craggs, J. Electron. Control **3**, 194 (1957).
[22] J. B. A. Mitchell, Phys. Rep. **186**, 215 (1990).
[23] S. G. Lias, J. E. Bartmess, J. F. Liebman, J. L. Holmes, R. D. Levin, and W. G. Mallard, J. Phys. Chem. Ref. Data **17** (Suppl. 1), 1 (1988).
[24] Y. Ikezoe, S. Matsuoka, M. Takabe, and A. Viggiano, *Gas Phase Ion-*

Molecule Reaction Rate Constants Through 1986 (Mass Spectroscopy Society of Japan, Tokyo, 1987).

[25] NIST Chemical Kinetics Database 17, version 2Q98, see: http://kinetics.nist.gov/index.php.

[26] W. S. Hwang, J. Chen, and W. J. Yoo, J. Vac. Sci. Technol. A **23**, 964 (2005).

[27] C.-Y. Sin, B. H. Chen, W. L. Loh, J. Yu, P. Yelehanka, A. See, and L. Chan, J. Vac. Sci. Technol. B **20**, 1974 (2002).

[28] C.-Y. Sin, B. H. Chen, W. L. Loh, J. Yu, P. Yelehanka, A. See, and L. Chan, AIChE J. **50**, 1578 (2004).

[29] T.-F. Yen, C. M. Chiu, and K. F. Chiu, Microelectron. Eng. **75**, 201 (2004).

[30] S. Mathew, R. Nagarajan, L. K. Bera, F. H. Hua, D. A. Yan, and N. Balasubramanian, Thin Solid Films **63**, 462 (2004).